

# Ability of the e-TellTale sensor to detect flow features over wind turbine blades: flow separation/reattachment dynamics

A. Soulier<sup>1,2</sup>, C. Braud<sup>2</sup>, D. Voisin<sup>1</sup>, B. Podvin<sup>3</sup>

*1- Mer Agitée, Route de Port-la-Forêt, 29940 La Forêt-Fouesnant*

*2- LHEEA (CNRS/ECN), Ecole Centrale Nantes 1, rue de la Noë, 44321 Nantes*

*3- LIMSI (CNRS), Campus Univ. bât. 507, Rue John Von Neumann, 91400 Orsay*

---

## Abstract

Monitoring the flow features over wind turbine blades is a challenging task that has become more and more crucial. This paper is devoted to demonstrate the ability of the e-TellTale sensor to detect the flow separation/reattachment dynamics over wind turbine blades. This sensor is made of a strip with a strain gauge sensor at its base. The velocity field was acquired using TR-PIV measurements over an oscillating thick blade section equipped with an e-TellTale sensor. PIV images were post-processed to detect movements of the strip, which was compared to movements of flow. Results show good agreement between the measured velocity field and movements of the strip regarding the separation/reattachment dynamics.

---

## 1. Introduction

Wind turbines are placed in the low layers of the atmospheric boundary layer where the wind is strongly influenced by the surface roughness and the thermal stability which creates turbulence and vertical gradients of the wind [9]. The rotor yaw and the blade pitch alignment within this highly unsteady wind inflow is a subject that is becoming more and more crucial with the rotor

blade lengths that are increasingly long (107m for the largest existing turbine: Heliade-X). Also, offshore turbines are arranged in an array layout and not just in-line, which induces additional sheared inflow conditions and additional small turbulent structures [5]. This results in strong and local variations of speed and directions on the wind turbine rotor blades. These variations lead to unsteady aerodynamic effects with turbulent inflows responsible of more than 65% of fatigue loads [22]. To alleviate these loads, smartblades and/or fluidic actuators are nowadays considered [19, 12, 2]. For this last strategy or to perform blade remote monitoring, one key issue is the development of robust technologies that are able to provide an instantaneous detection of the state of the flow on the blade aerodynamic surface. On current operating wind turbines the wind is generally monitored using an anemometer situated on the nacelle. It provides a slow measure of the wind which is perturbed by the rotor and the nacelle. Moreover being only a one-point measurement, it does not appreciate shear, yaw/pitch misalignments or turbulence on blades. Recent monitoring technologies allow to overcome some of these drawbacks. Among the most mature technologies, the spinner anemometer is measuring the wind in front of the rotor, removing perturbations from the rotor [21]. Also, capabilities, costs and integration of nacelle-mounted LIDAR, measuring the wind inflow few diameters upstream of the rotor, have been significantly improved during the last decades [1] [3]. However, from the knowledge of the authors, nothing is yet able to measure the state of the flow on current blades. Some field measurement campaigns were punctually performed for research purposes using pressure probes around the blades on dedicated blade manufacturing with however only weak potential of these sensors to be used in a day-to-day operation of wind turbines [26]. Some solutions were explored such as tufts or stall flags glued on the blade correlated with positions of the flow separation [25, 20][7]. However, these methods need a

mounted camera on the turbine with its associated drawbacks (fragility of the camera, vision at night ...).

An interesting alternative to these technologies is the electronic telltale sensor, developed by Mer Agitée<sup>1</sup>. It is composed of a strip moving like a tuft but with a strain gauge encased in its base making it able to transmit the information directly to any monitoring or control system through an embedded wireless electronic unit. It has been originally developed to detect flow separation on sails of offshore racing sailing vessels and has been recently adapted for wind turbine blade monitoring. Robustness and practical mounting issues were solved from industrial tests (figure 1a), while full scale tests of the device were performed at high Reynolds numbers in the wind tunnel facility of CSTB to demonstrate the relation between the e-Telltale sensor signal and the lift curve for static variations of the angle of incidence as can be seen in figure 1b [24]. The present study is intended to study the ability of the e-TellTale sensor to dynamically detect the flow separation/reattachment phenomena. For that purpose, experiments at a downscaled 2D blade section were performed in the LHEEA aerodynamic wind tunnel, using Time Resolved PIV and different post-processing methods to extract the strip position of the sensor in the flow field (vision algorithms) and to evaluate the flow separation over the aerodynamic surface (POD, and vortex detection). The experimental set-up and the post-processing methods are described in paragraph 2 and 3 respectively. Results are presented in the 4th paragraph including: a description of the baseline flow (4.1), results of the different post-processing methods to detect the flow separation (4.2), results on the ability of the e-TellTale sensors to detect flow separation (4.3).

---

<sup>1</sup><https://www.meragitee.com/>

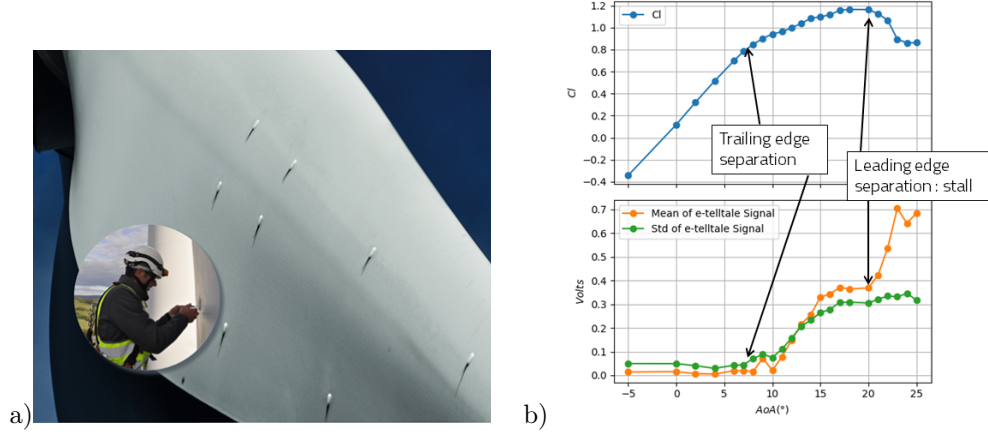


Figure 1: Previous studies: a) Robustness and practical mounting issues solve on EDF-Renewable wind turbines b) Ability of full scale e-TellTale sensors to detect static flow separations at high chord Reynolds numbers ( $10^6$ ) from wind tunnel tests

## 2. Experimental Setup

The experiments were performed in the recirculating aerodynamic wind tunnel facility of the LHEEA laboratory at Centrale Nantes (France). The working section is  $0.5 \times 0.5 \text{ m}^2$  and 2.4m long with a turbulent intensity less than 0.3% of turbulence. The Reynolds number based on the chord length of the 2D blade section,  $c \approx 0.09 \text{ m}$ , is  $Re_c = (U_\infty c) / \nu \simeq 2.10^5$  with  $U_\infty = 35 \text{ m/s}$  the free-stream velocity.

### 2.1. Blade profile

Measurements were performed using a NACA 65-421 profile in composite material. Due to the fabrication process, it is truncated at 91% of the chord length so that the trailing edge thickness is 2 mm (see figure 2). A similar profile was already used by Jaunet & Braud[12] to demonstrate the ability of local micro-jets to alleviate loads. It is a thick profile with two drops on the lift coefficient curve corresponding to a first boundary layer separation at the trailing edge of the profile for  $AoA \sim 8^\circ$ , and a second flow separation at the leading edge for  $AoA \sim 20^\circ$  causing stall. From  $8^\circ$  to  $20^\circ$  the separation point





Figure 2: NACA 654-421 profile manufactured in red and the theoretical trailing edge in black

moves gradually from the trailing edge to the leading edge, corresponding to a gradual variation of the loads.

An oscillating motion was imposed using a crank drive for the linear movement imposed by a feedback linear motor from LinMot. This oscillating motion was checked from PIV image processing using the detection of the blade surface at the position of the e-Telltale sensor. The detection of the blade surface was also later used to extract the position of the e-TellTale sensor in the vector field (see section 3.1). The amplitude of the blade oscillation,  $\Delta\alpha_0=5^\circ$ , was chosen so that the flow, initially separated at the trailing edge, moves gradually towards the leading edge flow separation where the stall occurs (see PIV vector fields in figures 8 and 9). The oscillating frequency,  $f_{osc}=1\text{Hz}$ , was chosen similar to the study of Jaunet & Braud [12] to mimic a constant shear inflow. This leads to a reduced frequency of  $k = \pi f_{osc} c / U_\infty = 0.008$  corresponding to a quasi-steady stall behavior [6]. The blade was equipped with a e-telltale sensor at mid-span on the suction side. Figure 3b) shows the e-telltale on the surface of the 2D blade profile installed in the LHEEA aerodynamic wind tunnel. A small part ( $\simeq 5\text{mm}$ ) of the pink strip of the e-telltale sensor is glued on a strain gauge sensor, itself glued on a thin stainless steel sheet embedded into the blade. The rest of the strip is free to move above the aerodynamic surface. Its length is one third of the blade chord. The signal from the strain gauge sensor was not acquired during PIV measurements, however, it was checked that the signal from this strip, made of a nylon fabric, behaves similarly as full-scale experiments from

[24]. In particular it was checked that we are able to distinguish the level of the signal when the sensor is in the two different flow states over the aerodynamic surface: attached / separated.

## 2.2. PIV measurements

Flow data were collected with a TR-PIV system able to produce 1600 velocity fields each second. A DM20-527 DH laser from Photonics Industries delivering a 2x20 mJ double laser sheet at the green wavelength of 527 nm was used in this setup. The camera was a Phantom Miro M310, recording 1200 x 800 px<sup>2</sup> images at 3200 Hz, the 6Gb of Ram memory of the camera allowed to capture 2000 velocity fields for each run. The camera was equipped with a Zeiss Makro Planar 2/50 lens (i.e.  $f = 50\text{mm}$ ,  $a = f/2$ ). With this setup, the field of view was 216 x 106 mm<sup>2</sup> leading to a spatial resolution of 6.3 px/mm. The PIV velocity fields were computed using a 16 x 16 px<sup>2</sup> interrogation area with an overlap of 50% leading to a grid resolution of 159 x 99 with a maximum spacing between vectors of 1.3mm or 0.014c. As seen in the figure 3 the optical axes of the camera was not totally perpendicular to the laser sheet. After calibrating this misalignment by taking snapshots of the calibration target, all the raw images and the velocity fields were dewarped. In addition to the classical noise inherent to PIV measurement, the presence of the e-telltale strip in the field of view of the PIV camera caused some spurious vectors explained by some light shoots on images when the clear fabric of the strip reflect the laser light directly towards the camera. To remove and replace these spurious vectors the automated post-processing algorithm developed by Garcia [10] was used.

## 3. Introduction in processing Methods

### 3.1. Strip detection method

The flow field over the aerodynamic surface is measured using TR-PIV measurements during the oscillations of the blade profile. To extract movements

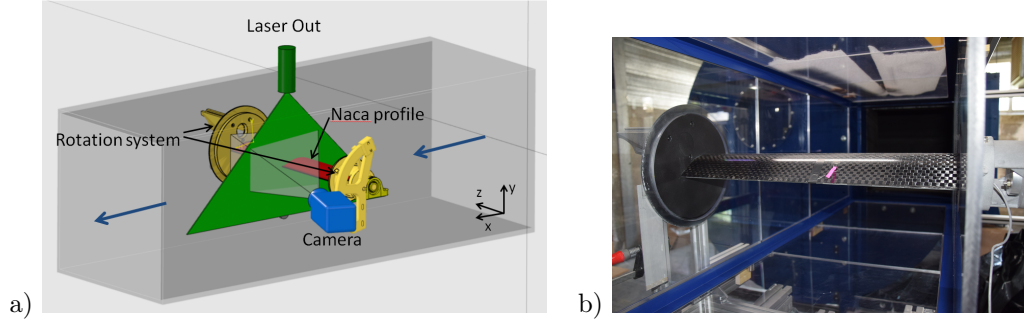


Figure 3: a) Scheme of the PIV set-up with the axes  $(x,y,z)$ . b) : The 2D blade section mounted in the LHEEA aerodynamic wind tunnel with the e-telltale in pink

of the e-TellTale strip within this flow field, PIV images were post-processed using vision algorithms from the Open Source Computer Vision Library<sup>2</sup>. The chosen methodology uses PIV images containing laser reflections of the blade surface and of the strip. The first step is to separate the blade surface contour from the strip contour. The images were first binarized so that white pixels, corresponding to the reflection of the laser on the blade and the strip surfaces, are set to 1 and all others to 0. To separate pixel coordinates of the blade from pixel coordinates of the strip, a local gradient of white pixel coordinates is computed, revealing ordinates of pixels corresponding to the strip location. Then, the resulting curve was smoothed using a Savitzky-Golay filter. Finally, this resulting identified profile curve was fit to the theoretical suction side profile curve to extract the best euclidean transformation (i.e. only rotation, translation and uniform scaling considered for the transformation) going from the measured curve to the theoretical profile. This was done using a function of OpenCV which primarily uses the RANSAC algorithm to detect spurious points and then the Levenberg-Marquardt algorithm to fit the profile. The result is a transformation matrix from which an angle of rotation is extracted. Also,

---

<sup>2</sup><http://opencv.org>

from the detected blade surface contour, a mask is defined to remove everything below it so that the remaining bright contour is the strip. The resulting cleaned binarized images were then used to extract the strip location using a contour detection function from OpenCV. The contour detection function recognize the white pixels surrounded by other white pixels and regroup all of it in one entity. As we are interested in the flow separation phenomena over the aerodynamic surface which induces large movements of the strip from the downstream to the upstream flow direction, it was found sufficient to resume the position of the strip by the center position of the detected contour. The strip detection method was first checked visually on some samples such as the figure 4 which shows raw PIV images on which the detected aera is circled in blue with the coordinate of its center noted  $sx$  and  $sy$  for the respective streamwise and spanwise directions. It was then possible to automatize the method for images of the oscillating blade periods. Missing values present in the signal are related to default in the contour detection algorithm as can be seen in the figure 4c. These outliers are found to be correlated with AoA beyond stall, where 3D effects are dominants. These values were replaced by the maximum value of  $sx$ . The corrected signal,  $sxc$ , is presented with the original signal  $sx$  in the figure 5.

### 3.2. Vortex identification method

Vortex identification methods are widely spread in the literature (see e.g. [13]). As they enable to distinguish swirling motion from shearing motion, they were developed to help in the understanding of turbulent flows and more recently as a real-time processing method for flow control purposes (see e.g. [4]). In the present study, the  $\Gamma_1$  criterion method is used [16]. This is a geometrical criterion defined as follows:

$$\Gamma_1(P) = \frac{1}{N} \sum_S \frac{(PM \wedge U_M) \cdot z}{\|PM\| \cdot \|U_M\|} \quad (1)$$

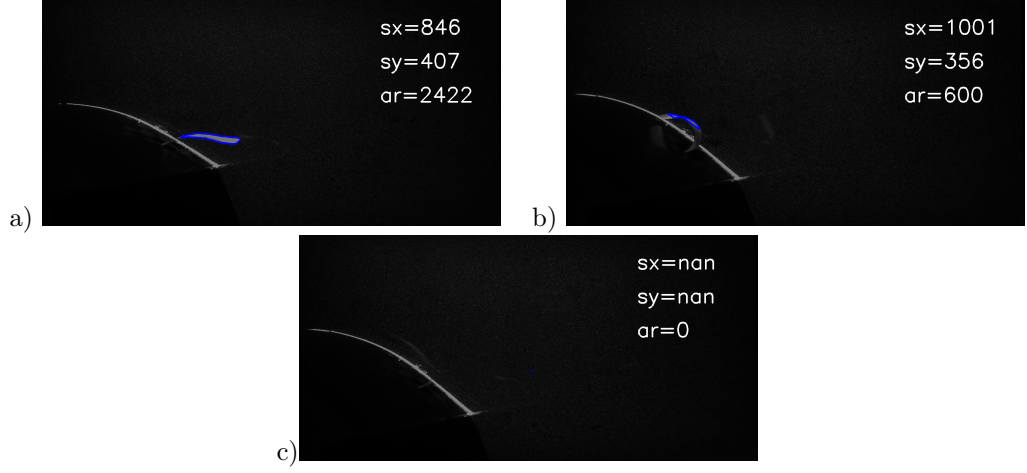


Figure 4: Detected strip contour from PIV images using OpenCV: a) for the attached flow case and b) for the detached flow case c) corresponding to an outlier case (impossible to detect the strip position).  $sx$  and  $sy$  are respectively the streamwise and spanwise positions in pixels of the center of the detected area (in blue).  $ar$  is the area of the detected contour in pixels

where  $N$  is the number of  $M$  points of the square area  $S$  around the center  $P$ ,  $U_M$  the velocity at the point  $M \in S$  and  $z$  the normal unit vector. The size of  $S$  act as a spatial filter. For this study different sizes of  $S$  from 9 to 3 grid points were tested and the differences were found not significant. The presented results were obtained with  $S$  being a square of 7 points. From this definition,  $\Gamma_1$  is a dimensionless scalar ranging from  $-1$  to  $1$ , which local extremum indicates the center of a vortex. Compared to other methods such as the well known  $Q$  criteria, the  $\Gamma_1$  criteria provides equivalent results, with the advantages to avoid computation of gradients (i.e. decreasing noise) and to provide the sign of vortices. Similarly as Mulleners and Raffel (2013) [18], the vortex identification method was used to extract vortex locations in the shear areas over the blade surface during the blade oscillation cycles (see figure 6 for an illustration of an instantaneous  $\Gamma_1$  field).

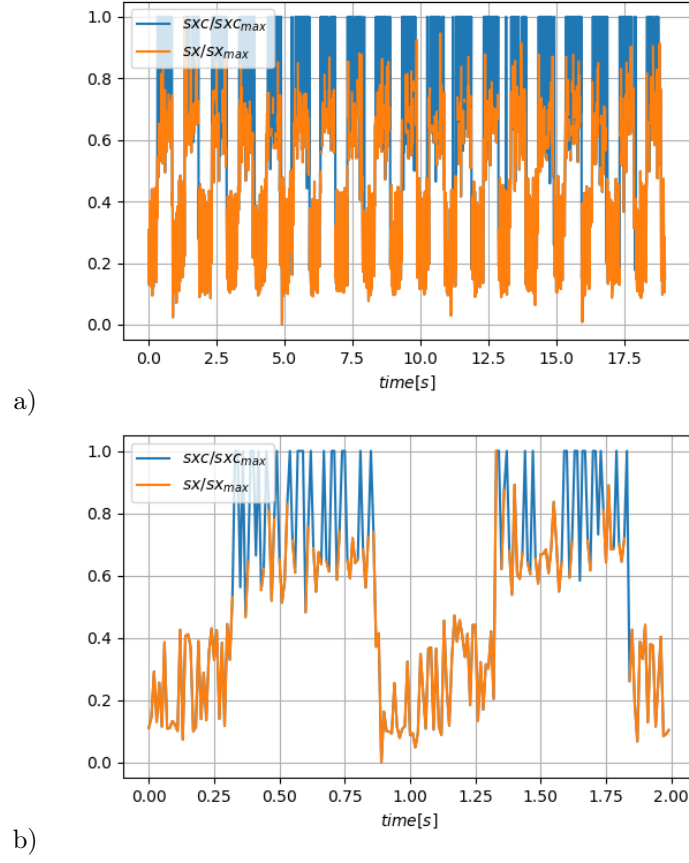


Figure 5: Streamwise coordinate of the identified strip  $sx$  before correction and  $sxc$  after correction a) the full run and b) a zoom on the two first oscillations

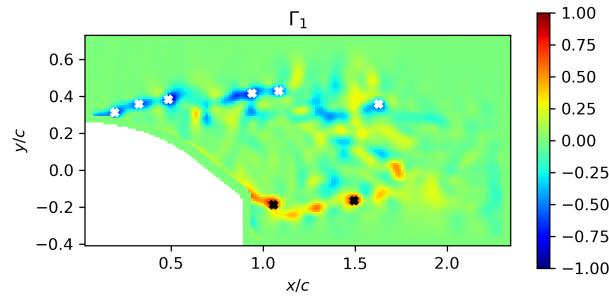


Figure 6: Instantaneous isocontour map of the  $\Gamma_1$  field with peaks identified using white cross markers for clockwise vortices and black cross markers for anticlockwise vortices

### 3.3. Proper Orthogonal Decomposition

The Proper Orthogonal Decomposition (POD), is a statistical technique [11] that extracts spatial modes  $\underline{\Psi}(\underline{x})$  that are best correlated on average with a given field  $\underline{u}(\underline{x}, t) = (u, v)$  defined on a domain  $\Omega$ . Let  $\langle . \rangle$  denote the temporal average. The field  $\underline{u}(\underline{x}, t)$  can be written as a superposition of spatial modes whose amplitude varies in time

$$\underline{u}(\underline{x}, t) = \langle \underline{u}(\underline{x}, t) \rangle + \sum_n a^n(t) \underline{\Psi}^n(\underline{x})$$

The modes can be identified with the method of snapshots [23], which is based on the computation of the temporal autocorrelation  $C$  for a given set of  $N$  snapshots  $\underline{u}(\underline{x}, t_i), i = 1, \dots, N$ :

$$C_{nm} = \int_{\Omega} \tilde{\underline{u}}(\underline{x}, t_n) \tilde{\underline{u}}(\underline{x}, t_m) d\underline{x},$$

where  $\underline{u}$  represents the fluctuating part of the snapshots ( $\tilde{\underline{u}}(\underline{x}, t_n) = \underline{u}(\underline{x}, t_n) - \langle \underline{u}(\underline{x}, t) \rangle$ ). The temporal amplitudes are eigenfunctions of

$$C_{nj} a^p(t_j) = \lambda^p a^p(t_n)$$

They are uncorrelated and their variance is given by

$$\langle a^n a^m \rangle = \lambda^n \delta_{nm}.$$

The spatial modes are then obtained from

$$\underline{\Psi}^n(\underline{x}) = \sum_{i=1}^N a^n(t_i) \underline{u}(\underline{x}, t_i).$$

By construction, the modes are orthonormal

$$\int_{\Omega} \underline{\Psi}^n(\underline{x}) \cdot \underline{\Psi}^m(\underline{x}) d\underline{x} = \delta_{nm}.$$

POD was applied to the 2-D PIV vector fields over two different domains. The largest domain is used in the description of the baseline flow (section 4.1), while the smaller domain is used to detect the flow separation/reattachment dynamics in the oscillating cycle (see section 3.1)

#### 4. Results

Results are presented in three steps. Firstly, the baseline flow is described, including a description of the flow during an oscillation cycle and the description of the secondary oscillation in the wake flow when separated. Then, three methods to detect the flow separation from PIV measurements are presented and compared. At last, results of the detection of the strip are compared to these methods to evaluate the ability of sensor to detect the flow separation.

##### 4.1. The baseline flow

One period of the blade oscillation relative angle,  $\Delta\alpha$ , is extracted using the blade contour mask from PIV images as explained in section 3.1 (see figure 7). The time duration  $T$  and the amplitude of the blade oscillation were chosen to include the flow separation phenomena for quasi-static stall conditions, as previously described in section 2.1. Points of interest within this oscillating period are marked with letters from (a) to (i) and the corresponding instantaneous vector fields are presented in figures 8 and 9. At the beginning of the oscillating period,  $\Delta\alpha = 0^\circ$  and  $t/T=0$ , the flow is slightly separated at the trailing edge of the profile as can be seen in figure 8a. From point (a) to (c), corresponding to a positive blade incidence variation, the separation point moves gradually from the trailing edge to the leading edge of the profile and the wake width increases accordingly as illustrated from 8a to 8b. From point (c) to point (d) the separation point suddenly moves towards the leading edge with a corresponding increase of the wake width, until the flow is fully separated over the aerodynamic



profile (see figure 8c and d). This last phenomena is ten times faster than the previous one and is clearly related to the stall phenomena. From point (d) to point (e), the flow past the blade can clearly be considered as a wake flow with a separation that occurs on both sides of the blade, the leading and trailing edges (see figure 8d and e).

From point (e) to (g), despite the progressive decrease of the adverse pressure gradient on the suction side of the blade through a negative variation of the blade incidence during 0.3 seconds, the flow remains fully separated (see figure 9 e, f and g). From point (g) to point (h), corresponding to a duration of  $\Delta t = 0.02s$ , the separation point suddenly moves back towards the trailing edge. Again, this phenomena is ten times faster than the time duration from (e) to (g) for which the blade incidence is progressively decreasing (see figure 9 g and h). From point (h) to (i), the separation point is back to its initial state (see figure 9 h and i). The stall and reattachment instants are defined respectively as  $t_{stall}^{ref}(ic) = (t_c + t_d)/2$  and  $t_{attach}^{ref}(ic) = (t_g + t_h)/2$  with  $t_c$ ,  $t_d$ ,  $t_g$  and  $t_h$  the instants (c), (d), (g) and (h) extracted from  $ic = 1$  to  $N_{cycle}$ ,  $N_{cycle} = 18$  being the total number of instantaneous oscillation cycles. They will be used in the following as a reference for the flow separation/reattachement detection methods of section 4.2.

It should be emphasize that the separation/detachment phenomena has a time scale corresponding to  $\sim 10c/U_\infty$  in good agreement with the theoretical work of Jones [14], with a separation/detachment location which occurs within one third of the blade chord from the leading edge.

To characterize further the coherent structure organization during this blade oscillation cycle, a POD analysis is performed from a database coming from a higher PIV acquisition rate, 1600Hz. All vector fields of the blade oscillation cycles are used for the computation of the temporal autocorrelation coefficient

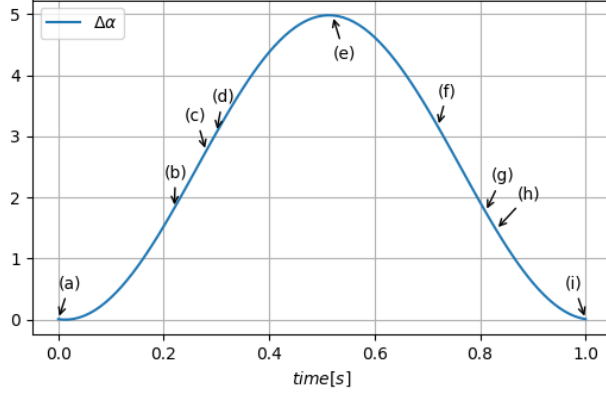


Figure 7: Evolution of the relative angle of attack  $\Delta\alpha$ . (x) : instantaneous velocity fields detailed below

$C$  (see section 3.3), corresponding to 2000 snapshots. The convergence of the resulting POD decomposition, in term of the relative energy content with modes, is presented in figure 10 using the following definition :

$$\Lambda_i = \frac{\lambda_i}{\sum_{j=1}^N \lambda_j}$$

where  $N$  is the number of modes and  $\lambda_i$  the eigenvalue of the  $i$ th-mode.

As highlighted from figure 10, the dominant modes in term of energy content are the three first POD modes, with around 14% of kinetic turbulent energy for the first mode, 10% for mode 2 and of 8% for mode 3. These three modes are represented in figure 11 using the spatial modes,  $\underline{\Psi}^n(\underline{x})$  with  $n = 1, 2, 3$ , together with the temporal modes scaled with the associated energy content,  $a^n(t)/(2\lambda^n)$  with  $n = 1, 2, 3$ . The first mode is phased with the blade oscillation period and clearly captures variations of the mean velocity deficit in the wake due to these oscillations. The second and third modes exhibit structures in the wake which could be associated to the vortex shedding organization, typically found in the wakes of bluff bodies. Following the work of Yarusevych et al (2009) [27], the Strouhal number  $St = f_s d / U_\infty \sim 0.22$  is extracted, with  $f_s$  the peak frequencies

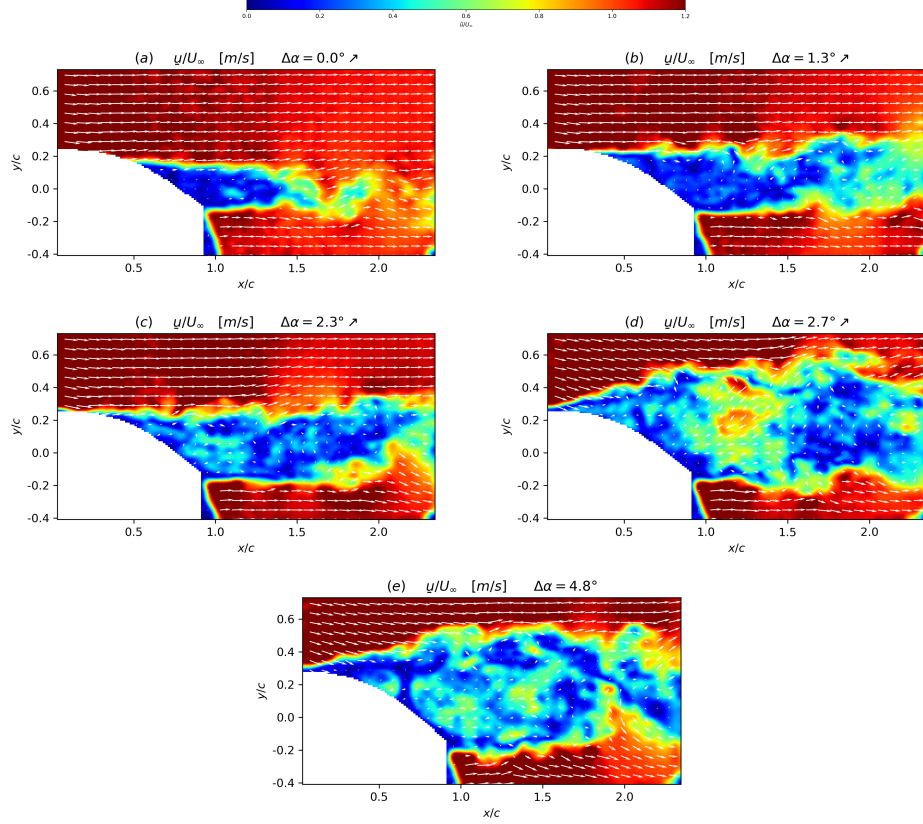


Figure 8: Instantaneous velocity fields superposed with isocontours of the velocity modulus (i.e.  $\sqrt{\|u\|^2 + \|v\|^2}$ ) at different  $\Delta\alpha$  corresponding to points of the blade oscillation given in figure 7 during the upstroke phase (noted  $\nearrow$ ): (a) is a point at the lowest  $\Delta\alpha$  of the upstroke phase of the oscillation cycle, (b) is an intermediate point, (c) is a point just prior to full stall angle, (d) is a point just after the stall angle and (e) corresponds to a point at the maximum amplitude of the blade oscillation cycle

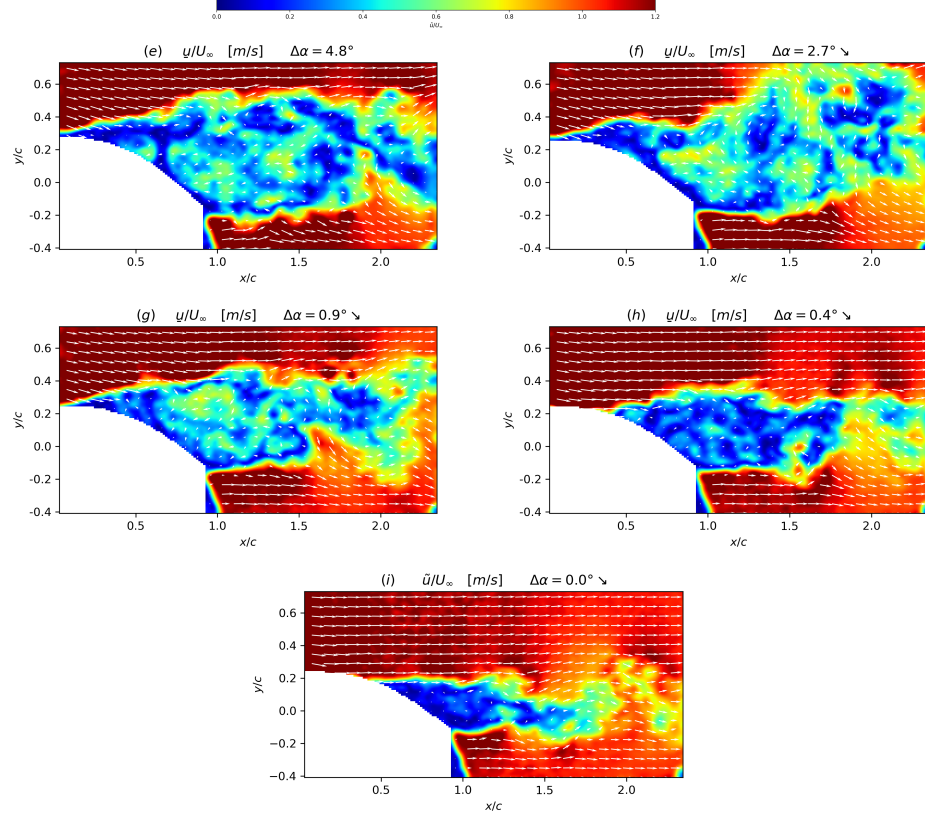


Figure 9: Instantaneous velocity fields superposed with isocontours of the velocity modulus (i.e.  $\sqrt{\|u\|^2 + \|v\|^2}$ ) at different  $\Delta\alpha$  corresponding to points of the blade oscillation given in figure 7 during the downstroke phase (noted  $\searrow$ ): (e) corresponds to a point at the maximum amplitude of the blade oscillation cycle, (f) is an intermediate point, (g) is a point just prior to the flow reattachment, (h) is a point just after the flow reattachment and (i) is a point similar at the lowest  $\Delta\alpha$  of the downstroke phase

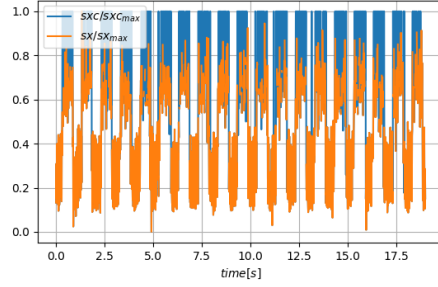


Figure 10: Energy content of each of the first 50 POD modes

from the FFT of temporal modes,  $a^n(t)/(2\lambda^n)$  with  $n = 2, 3$ , and  $d$  a measure of the wake width using the vertical distance between the two local maximum of the *r.m.s* of the streamwise velocity at  $x/c = 1.25$ . This Strouhal number is of the same order of magnitude of the one found by Yarusevych et al (2009) [27] behind the wake of a NACA 0025 airfoil at the angle of attack of  $10^\circ$  and clearly assess the link of these modes to the vortex shedding organization behind the blade wake (see figure 12).

#### 4.2. Detection methods

To be able to study the ability of the strip to detect the instants of the flow separation/reattachment, three robust detection methods were applied to the flow field obtained from the TR-PIV measurements:

- Method 1: using of the tangential instantaneous velocity component in the direction perpendicular to the surface as introduced by [8]
- Method 2: using the extraction of vortices in the shear layers as explained in section 3.2
- Method 3: using the POD decomposition introduced in section 3.3

In the perspective of using these sensors for real time control/monitoring purposes, the application of these methods to instantaneous signals is preferred.

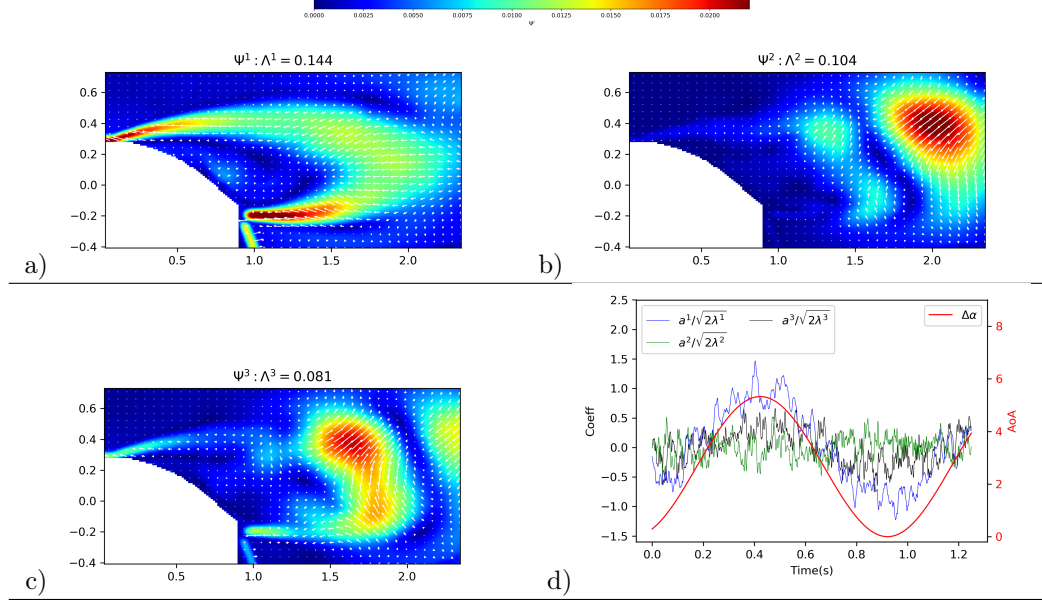


Figure 11: POD decomposition: a), b) and c) represents the eigenvectors vector field,  $\Psi_i^n, i = 1, 2$ , of the first three modes respectively ( $n = 1, 2, 3$ ) with isocontours of its modulus superimposed, the associated energy content of the  $n$  th mode (i.e.  $\Lambda^n$ ) being written in the title, d) represents the corresponding temporal coefficients scaled with their energy content

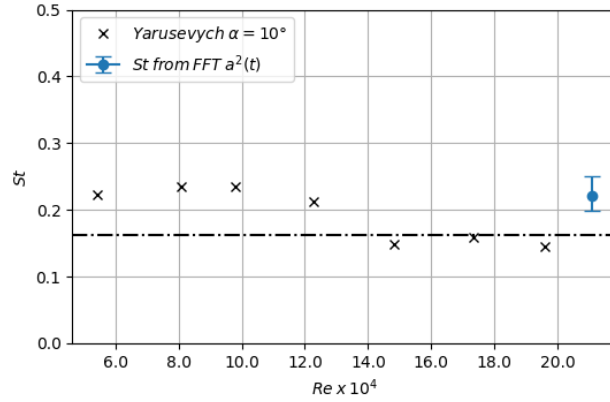


Figure 12: Strouhal number values extracted from [27] and from the FFT of the temporal mode,  $a^2(t)$ , of the POD decomposition

For each method a stall/reattachment criteria is defined, corresponding to a zero crossings criteria explained in the introduction of the first method (next section).

#### 4.2.1. Method 1

For the first method, the flow separation/reattachment instants are detected for each oscillating cycle using the normal profile of the instantaneous stream-wise velocity component at a position corresponding to the attached strip location  $x_{strip} = x/c \simeq 0.7$ ,  $U_{norm}(t_i, x_{strip}, y_b)$  with  $i$  the number of snapshots and  $y_b$  the direction normal to the blade surface. The chosen line location is presented in white on the figure 13a. The normal profile is then reduced to a single value by averaging in the normal direction,  $U_{norm}(t, x_{strip}) = \int_{y_b=0}^{l/c} U_{norm}(t, x_{strip}, y_b) dy_b$  with  $l/c \simeq 0.7$  the normalized integration length in the normal direction, chosen so that each instant (or each angle of incidence) corresponds to one value of this normal velocity. Different positions and integration lengths have been explored with no significant influence on the results. This could be partly explained from the fact that PIV measurements do not capture the boundary layer gradient from the aerodynamic surface. The phased average of the obtained  $U_{norm}(t)$  signal,  $\overline{U_{norm}}$ , is presented in figure 13b together with its gradient for further understanding of this detection method.

For low angles of incidence  $\overline{U_{norm}}/U_\infty \simeq 1$ , meaning  $\overline{U_{norm}}$  is close to the free-stream velocity which corresponds to an attached flow state over the aerodynamic surface. Similarly, for the large angles of incidence  $\overline{U_{norm}}/U_\infty$  is negative, bringing to light the reverse flow above the profile and thus the flow separation state. The time window width marked by green and red hatched areas corresponds to the standard deviation  $\sigma(t_{(stall-or-attach)}^{ref}(ic) - ic.T)$  centered on the averaged of the reference instants extracted from the instantaneous velocity fields of section 4.1,  $\overline{t_{stall}^{ref}(ic)}$  and  $\overline{t_{attach}^{ref}(ic)}$ . Gradient peaks are close to these

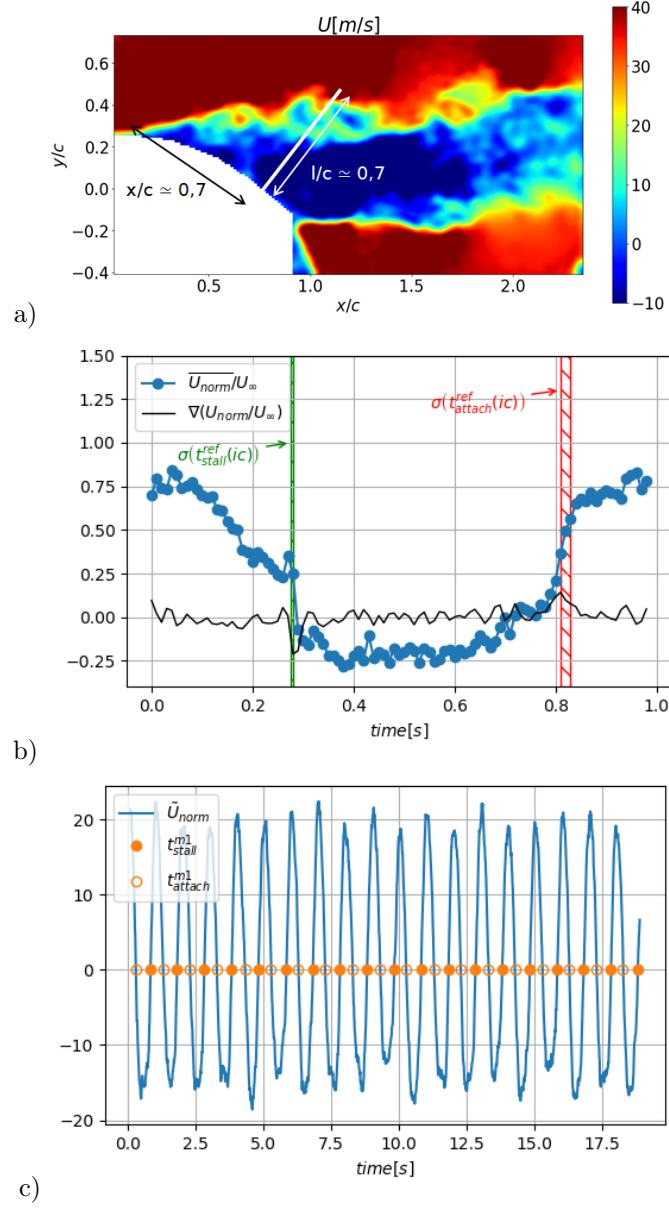


Figure 13: First method to detect the flow stall/reattachment instants: a) location and direction of integration line used to compute  $U_{norm}(t_i)$  (i.e. white bar on the blade) reported on isocontours of the velocity modulus from PIV measurements, b) The phased-averaged signal  $\bar{U}_{norm}$  with its gradient  $\nabla \bar{U}_{norm}$ , c) results of the zero-crossing method to extract the flow stall/reattachment instants using the first method. The filled circle symbols correspond to stall instants,  $t_{stall}^{m1}(ic)$ , and void circle symbols corresponds to reattachment instants,  $t_{attach}^{m1}(ic)$ .



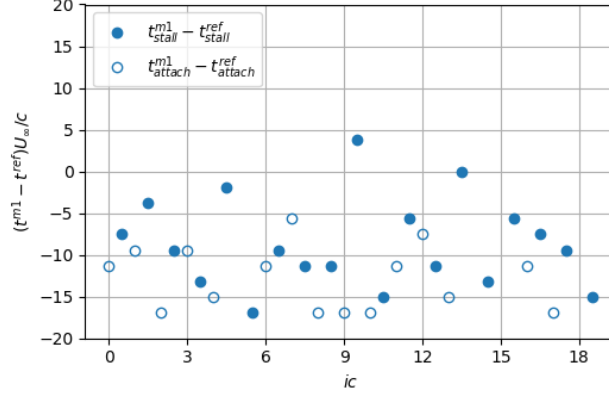


Figure 14: Normalized delay of the stall and reattachment detected instants using  $U_{norm}(t)$  (method 1)

reference instants which constitute a first validation of the method. To extract the stall or reattachment instants from the instantaneous  $U_{norm}(t, x_{trip})$  signal, defined respectively as  $t_{stall}^{m1}(ic)$  and  $t_{attach}^{m1}(ic)$ , it is first smoothed using a centered moving average algorithm using a filter width of 21 time steps. Then, a zero-crossing criteria is applied. This criteria uses the  $U_{norm}(t)$  signal removed by its mean value,  $\tilde{U}_{norm}(t)$ , so that sudden variations of the signal are located where the fluctuating signal is crossing the x-axis. Finally, the sign of the gradient,  $sign(\nabla U_{norm})$ , is used to discriminate stall instants from reattachment instants,  $t_{stall}^{m1}(ic)$  and  $t_{attach}^{m1}(ic)$  (see figure 13c). This zero-crossing method will be also used for the detection methods 2 and 3 that follows.

The resulting detected instants,  $t_{stall}^{m1}(ic)$  and  $t_{attach}^{m1}(ic)$  are compared to the reference instants extracted from the instantaneous velocity fields of section 4.1,  $t_{stall}^{ref}(ic)$  and  $t_{attach}^{ref}(ic)$  (see figure 14). The first observation is that the stall and reattachment instants are detected earlier in average,  $\frac{-8.6c}{U_{\infty}}$  and  $\frac{-15c}{U_{\infty}}$  chord time respectively (or 2.5 to 4 time steps), when using this first detection method. Then, a certain dispersion exist in the detected instants that can be quantified using the standard deviations,  $\frac{\sigma(t_{stall}^{m1}(ic) - ic.T)}{c/U_{\infty}} = 3.3$  and  $\frac{\sigma(t_{attach}^{m1}(ic) - ic.T)}{c/U_{\infty}} = 5.0$ .

It is found of the same order of magnitude as the reference case,  $\frac{\sigma(t_{stall}^{ref}(ic)-ic.T)}{c/U_\infty} = 2.1$  and  $\frac{\sigma(t_{attach}^{ref}(ic)-ic.T)}{c/U_\infty} = 7.0$ . Also, knowing the time resolution is  $3.5U_\infty/c$ , this dispersion should be attributed to the time accuracy of the dataset.

#### 4.2.2. Method 2

Another flow separation detection method is introduced with this time a criteria associated with physical grounds. Indeed, it is using the vertical distance between identified vortices in the separated shear layers forming the blade wake width, directly related to the flow separation location on the aerodynamic surface [27] (see 3.2 on the vortex identification method). The wake width is defined as :

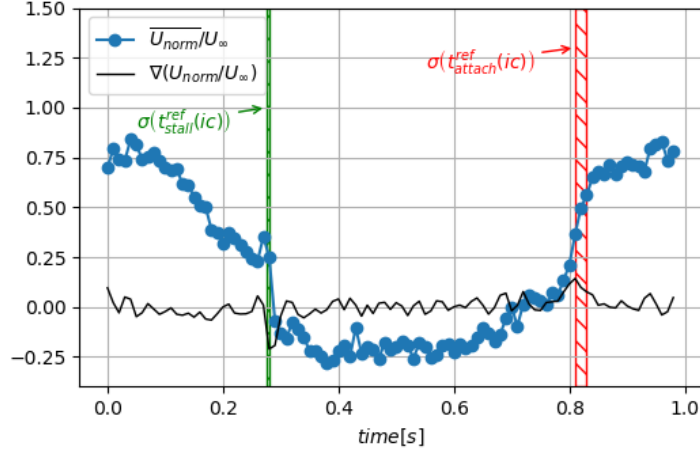
$$W(t) = \left| \frac{1}{N_{clock}(t)} \sum_{n=1}^{N_{clock}(t)} y_n(t) - \frac{1}{N_{anti-clock}(t)} \sum_{m=1}^{N_{anti-clock}(t)} y_m(t) \right| \quad (2)$$

with subscripts *clock* and *anti-clock* corresponding to quantities from the clockwise and anti-clockwise rotating vortices respectively and  $N$  the number of vortices identified at the time  $t$ . The obtained signal can be phased averaged,  $\overline{W(t)}$ , as presented in figure 15a. Gradient peaks of the  $\overline{W(t)}$  signal are close to the reference instants, which standard deviation is represented by green and red hatched areas. This constitute a first validation of the method. As for the first method, the zero-crossing criteria is applied to the resulting filtered temporal evolution of  $W(t)$  to obtain stall and separated instants,  $t_{stall}^{m2}(ic)$  and  $t_{attach}^{m2}(ic)$ . First results show that the mean detected stall instant is closer to the reference than the first detection method, i.e.  $\frac{-2.5c}{U_\infty}$  (less than one time step), while the reattachment instant is detected significantly earlier  $\frac{-18c}{U_\infty}$ . The dispersion in the detected instant computed using the standard deviation is of the order of 2 time steps for both the stall and the reattachment, i.e.  $\frac{\sigma(t_{stall}^{m2}(ic)-ic.T)}{c/U_\infty} = 6.8$  and  $\frac{\sigma(t_{attach}^{m2}(ic)-ic.T)}{c/U_\infty} = 7.8$ . The increased dispersion in the detected stall instants

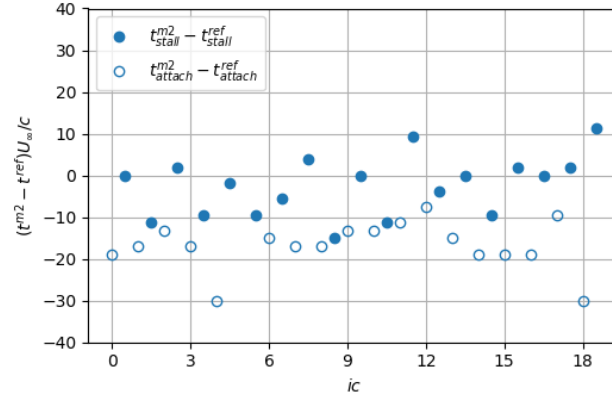
compared to the reference case should be attributed to the higher difficulty to detect shear layer vortices for instants before stall, for which vortices are smaller (i.e. within the spatial resolution of PIV measurements).

#### 4.2.3. Method 3

These two previous methods provide an instantaneous detection of the flow separation phenomena. To explore further the detection of these instants, we choose to use another method based on statistics introduced in section 3.3. It was already used in the context of wind energy for the analysis of the dynamic stall phenomena by Melius et al (2016) & Mulleners et al (2016) [15, 17]. The chosen vector field for the present analysis focuses on the separated shear layer dynamics rather than the wake dynamics from the initial PIV field of view (see figure 16). 2000 snapshots were used with no distinction of the phase, which enables to extract the flow separation state within the first POD modes as explained by [15, 17]. As a first approach, the phased average of the two first POD modes are presented in figure 17 with temporal coefficients  $a^1(t)$  and  $a^2(t)$ . The first mode of the eigenvector field presented in figure 17a (i.e.  $\Psi_i^1, i = 1, 2$ ), contains 77% of the total turbulent kinetic energy (i.e.  $\Lambda^1 \sim 0.77$ ) and captures accelerations and deceleration of the flow over the profile depending on the sign of the associated temporal coefficient  $a^1(t)$ . The transitions between the accelerations (i.e.  $a^1(t) < 0$ ) and deceleration (i.e.  $a^1(t) > 0$ ) phases is marked by abrupt variations of amplitudes, which should be associated to instants of the stall and the flow reattachment phenomenon. The second mode of the eigenvector field presented in figure 17b (i.e.  $\Psi_i^2, i = 1, 2$ ), contains much less turbulent kinetic energy (i.e.  $\Lambda^2 \sim 0.049$ ) and exhibits a shear layer with a shear direction that is changing accordingly with the sign of its associated temporal coefficient  $a^2(t)$ . This variation of shear may be associated to the passage of the famous dynamic stall vortex created during unsteady variations of



a)



b)

Figure 15: Second method to detect the flow stall/reattachment instants: a) The phased-averaged signal  $\overline{W}(t)$  with its gradient  $\nabla \overline{W}(t)$ , b) results of the zero-crossing method to extract the flow stall/reattachment instants using the second method,  $t_{stall}^{m1}(ic)$  and  $t_{attach}^{m1}(ic)$ , compared to reference instants. The time window width marked by green and red hatched areas corresponds to the standard deviation  $\sigma(t_{(stall-or-attach)}^{ref}(ic) - ic.T)$  centered on the averaged of the reference instants extracted from the instantaneous velocity fields of section 4.1,  $\overline{t_{stall}^{ref}}(ic)$  or  $\overline{t_{attach}^{ref}}(ic)$ . The filled circle symbols correspond to stall instants, and void circle symbols corresponds to reattachment instants.

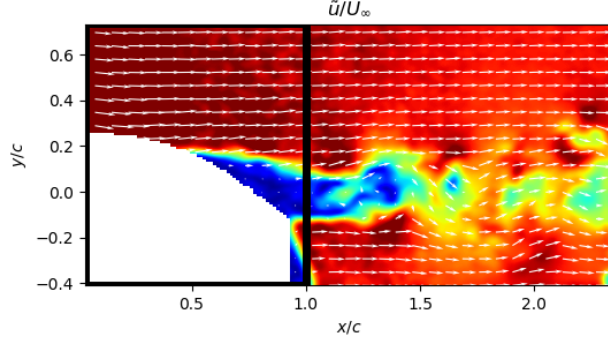


Figure 16: Reduced field of view (black rectangle) used for the third detection method using POD.

the angle of incidence as pointed out by [15, 17]. Interestingly, minimums of  $a^2(t)$  occurs significantly ahead of the flow separation/reattachment instants contrary to the first mode. However, studying the ability of the e-telltale sensor to detect dynamic stall vortex needs further investigations that won't be performed in this work. The following will therefore focus on the first POD mode.

The coefficient of the first mode  $a^1(t)$  was also studied instantaneously to compare with the other detection methods. A zero-crossing criteria was applied to this instantaneous signal, leading to detected stall and reattachment instants  $t_{stall}^{m3}(ic)$  and  $t_{attach}^{m3}(ic)$ . First results show these instants follows the trend of the first detection method regarding the mean quantities, i.e. the detection occurs earlier than the reference:  $\frac{-6.2c}{U_\infty}$  and  $\frac{-12c}{U_\infty}$ , and the dispersion is similar to the reference, i.e.  $\frac{\sigma(t_{stall}^{m3}(ic)-ic.T)}{c/U_\infty} = 1.7$  and  $\frac{\sigma(t_{attach}^{m3}(ic)-ic.T)}{c/U_\infty} = 5.7$ .

#### 4.3. Ability of the sensor to detect flow separation

Detection methods 1, 2 and 3 using TR-PIV measurements will be compared to the detection method using the e-TellTale sensor. For that purpose, the phase averaged strip position,  $\overline{sx(t)}$ , is detected from image processing as explained in section 3.1 and presented in figure 19 together with the time averaged standard deviation of stall and reattachment instants detected from the instantaneous

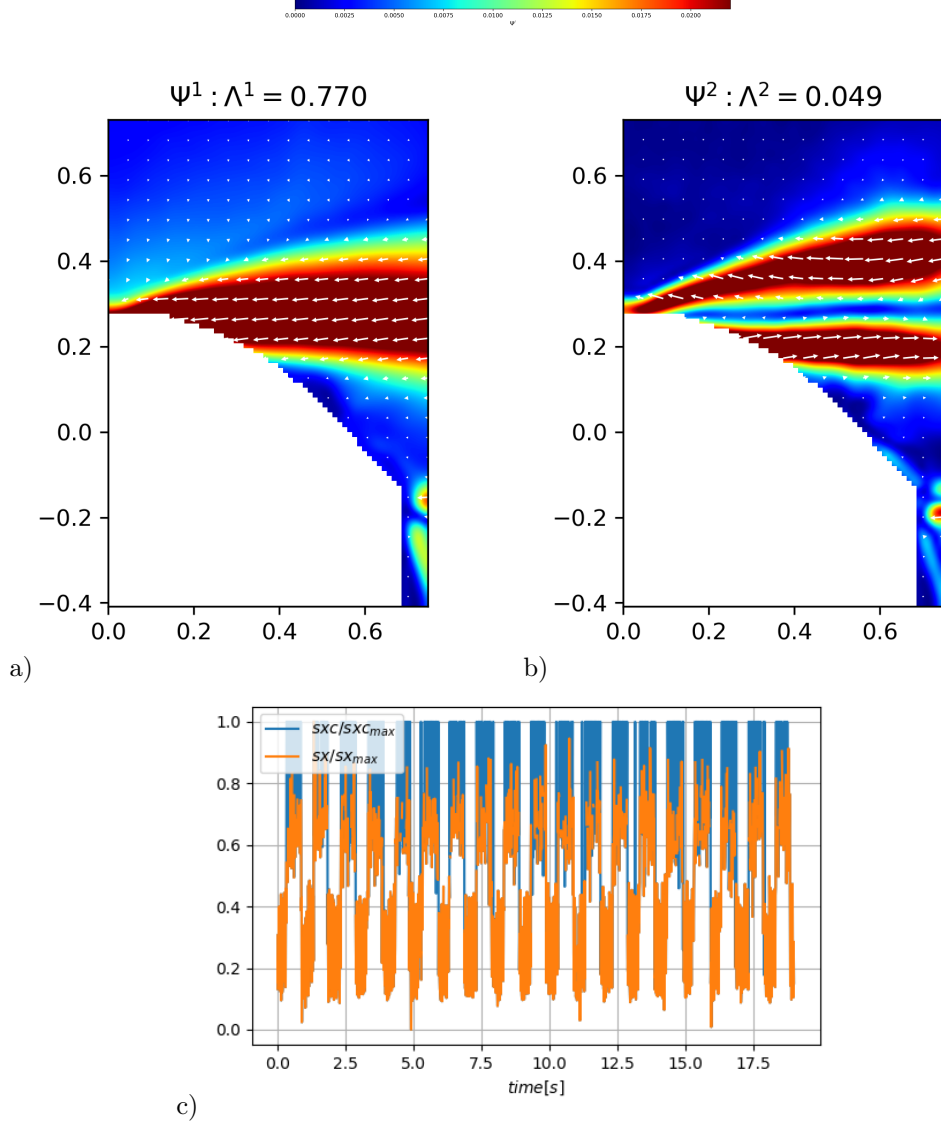


Figure 17: Third method to detect the flow separation/reattachment instants: a) and b) are isocontours of the eigenvectors field  $\Psi_i^n$ , with  $i = 1, 2$ , of the  $n$ -th mode, with isocontours of its modulus superimposed.  $\Lambda^n$  is the eigenvalue of the  $n$ -th mode, representing the part of the turbulent kinetic energy in the mode. c) represents the phase averaged of the corresponding temporal coefficients scaled with their turbulent kinetic energy content ( $a^n(t)/\sqrt{2\lambda^n}$ ,  $n = 1, 2$ ). The time window width marked by green and red hatched areas corresponds to the standard deviation  $\sigma(t_{(stall-or-attach)}^{ref}(ic) - ic.T)$  centered on the averaged of the reference instants extracted from the instantaneous velocity fields of section 4.1,  $\overline{t_{stall}^{ref}(ic)}$  or  $\overline{t_{attach}^{ref}(ic)}$ .

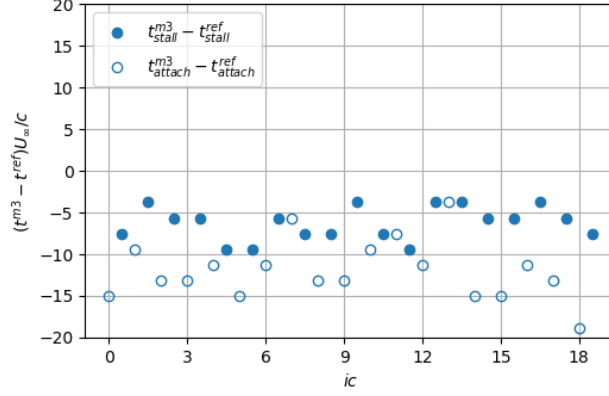


Figure 18: Results of the zero-crossing method to extract the flow separation/reattachment instants using the third method. The filled circle symbols correspond to stall instants,  $t_{stall}^{m3}(ic)$ , and void circle symbols corresponds to reattachment instants,  $t_{attach}^{m3}(ic)$

flow field (i.e. green and red hatched areas respectively). It is observed that the position of the strip during the oscillation cycle is characterized by two sudden changes, revealed with the gradient peaks, in very good agreement with the stall and reattachment instants observed with the instantaneous flow field. This is a first validation of the e-TellTale sensor to detect stall and reattachment instants.

To characterize further the detected instants from the movement of the strip, the zero-crossing criteria is applied to the instantaneous signal of the position of the strip,  $sx(t)$ . Resulting stall and reattachment instants removed by the reference instants,  $t_{stall}^{sx}(ic) - t_{stall}^{ref}(ic)$  and  $t_{attach}^{sx}(ic) - t_{attach}^{ref}(ic)$ , are plotted in figure 20. As highlighted here, the mean value is very close to the reference (i.e. close to zero). Furthermore, when compared to the detected instants from the three other methods summarized in tabular 1, the e-TellTale detection method presents the smallest delay to the reference, i.e.  $\frac{0.5c}{U_{\infty}}$  and  $\frac{-1.2c}{U_{\infty}}$ . Furthermore, the dispersion difference with the reference is within one time step, i.e.  $3.5U_{\infty}/c$ , from the reference case, i.e.  $\frac{\sigma(t_{stall}^{sx}(ic) - ic.T)}{c/U_{\infty}} = 5.2$  and  $\frac{\sigma(t_{attach}^{sx}(ic) - ic.T)}{c/U_{\infty}} = 3.3$ ,

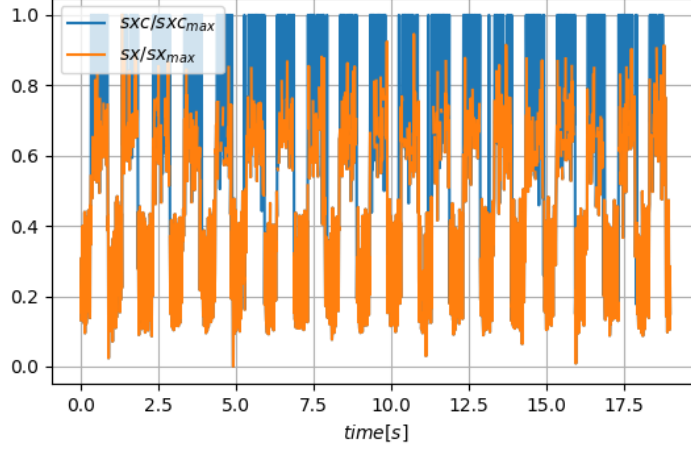


Figure 19: The evolution of dimensionless phase averaged streamwise coordinate of the center of the strip,  $sx/sx_{max}$ , during the oscillation cycle (blue dotted line) together with its gradient (black line) . The time window width marked by the red hatched area corresponds to the standard deviation  $\sigma(t_{stall}^{ref}(ic) - ic.T)$  centered on the averaged  $t_{stall}^{ref}(ic)$  . The time window width marked by the green hatched area corresponds to the standard deviation value  $\sigma(t_{attach}^{ref}(ic) - ic.T)$  centered on the phase averaged  $t_{attach}^{ref}(ic)$  .

which should be attributed to the time accuracy.

## 5. Conclusion

The ability of an original e-TellTale sensor to detect flow separation/reattachment instants during an oscillation of the angle of incident of a blade section has been explored. For that purpose, a 2D NACA 65-421 blade section equipped with a e-TellTale sensor at its trailing edge has been set in the LHEEA aerodynamic wind tunnel. The blade was oscillating around the stall angle to reproduce a constant shear inflow perturbations in front of a rotating wind turbine blade at a chord Reynolds number of  $2.10^5$ . Three methods to detect the flow separation/reattachment instants have been successfully applied using Time-Resolved-PIV measurements during the blade oscillation cycle. This includes two instantaneous methods, the direct use of the tangential instantaneous velocity (method 1) and the instantaneous extraction of shear layer vortices (method



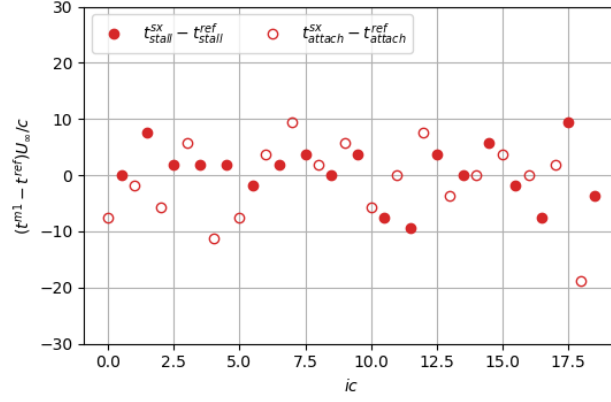


Figure 20: Comparison of the detected instants between the three methods using the instantaneous velocity fields and the position of the strip.

	Mean of delays between stall detection with the different methods and the reference (a)	Mean of delays between reattachment detection with the different methods and the reference (b)	Standard deviation of the detected instants of stall (c)	Standard deviation of the detected instants of reattachment (d)
Reference			2.1	7.0
Method1	-8.6	-15	3.3	5.0
Method2	-2.5	-18	6.8	7.8
Method3	-6.2	-12	1.7	5.7
Epenon	0.5	-1.2	5.2	3.3
a) : $\frac{\sum_{ic=1}^{N_{cycle}} (t_{stall}^{mj}(ic) - t_{stall}^{ref}(ic))}{N_{cycle} c / U_{\infty}}$ b) : $\frac{\sum_{ic=1}^{N_{cycle}} (t_{attach}^{mj}(ic) - t_{attach}^{ref}(ic))}{N_{cycle} c / U_{\infty}}$ c) : $\frac{\sigma(t_{stall}(ic) - ic.T)}{c / U_{\infty}}$ d) : $\frac{\sigma(t_{attach}(ic) - ic.T)}{c / U_{\infty}}$				

Table 1: Summarize of detected instants values using the three methods including: averaged detected instants compared to averaged reference instants and standard deviations . All times are expressed as chord times ( $t_c = c/U_{\infty}$ )

2), and one statistical method using POD (method 3). Method 1 and 3 were found equivalent, with an earlier detection of the stall/reattachment instants (2 to 4 time step earlier) and a dispersion in the detection similar as the reference case. Method 2, using an instantaneous vortex detection method, presents a detection of the stall closer to the reference that is however detected with a higher dispersion. This should be attributed to the difficulty to extract vortices when the flow is attached. The e-TellTale detection method presents the best results with a detection of the reference instants within less than one time step and a dispersion similar as the reference case. This study demonstrates the ability of the e-TellTale sensor strip to detect the instantaneous separation/reattachment dynamics over the blade. What remains to be done is a link between this dynamic strip position and the dynamic response of e-TellTale strain gauge signal. Also, the methodology used in the present paper is intended to be used in the extraction of other flow features over the blade surface such as the well known dynamic stall vortex or the blade wake dynamics.

### **Acknowledgement**

Authors would like to thanks Jean-Jacques Lasserre, Philippe Galtier for the PIV Dantec equipment loan and their assistance during measurements. We also would like to thanks Vincent Jaunet for his help during the PIV acquisition. This work was partly carried out within the framework of the WEAMEC, West Atlantic Marine Energy Community, and with funding from the city of Nantes, the Pays de la Loire Region and Centrale Nantes in France.

### **References**

- [1] S. Aubrun, E. T. Garcia, M. Boquet, O. Coupiac, and N. Girard. Wind turbine wake tracking and its correlations with wind turbine monitor-

- ing sensors. Preliminary results. *Journal of Physics: Conference Series*, 753:032003, 2016.
- [2] E. C. Batlle, R. Pereira, and M. Kotsonis. Airfoil Stall Hysteresis Control with DBD Plasma actuation. *55th AIAA Aerospace Sciences Meeting*, 2017.
  - [3] E. A. Bossanyi, A. Kumar, and O. Hugues-Salas. Wind turbine control applications of turbine-mounted LIDAR. *Journal of Physics: Conference Series*, 555:012011, 2014.
  - [4] C. Braud and A. Liberzon. Real-time processing methods to characterize streamwise vortices. *Journal of Wind Engineering and Industrial Aerodynamics*, 179:14–25, Aug. 2018.
  - [5] L. P. Chamorro, M. Guala, R. E. A. Arndt, and F. Sotiropoulos. On the evolution of turbulent scales in the wake of a wind turbine model. *Journal of Turbulence*, N27, 2012.
  - [6] A. Choudhry, R. Leknys, M. Arjomandi, and R. Kelso. An insight into the dynamic stall lift characteristics. *Experimental Thermal and Fluid Science*, 58:188–208, 2014.
  - [7] G. P. Corten. *Flow separation on wind turbines blades*. PhD thesis, University Utrecht, The Netherlands, 2001.
  - [8] F. De Gregorio, F. Albano, and L. M. Flow separation investigation by PIV technique. In *7th International Symposium on Particle Image Velocimetry*, Rome, Italy, 2007.
  - [9] S. Emeis. *Wind Energy Meteorology: Atmospheric Physics for Wind Power Generation*. Springer, 2018. Google-Books-ID: 6r1TDwAAQBAJ.
  - [10] D. Garcia. A fast all-in-one method for automated post-processing of PIV data. *Experiments in Fluids*, 50(5):1247–1259, 2011.

- [11] P. Holmes, J. L. Lumley, and G. Berkooz. *Turbulence, Coherent Structures, Dynamical Systems and Symmetry by Philip Holmes*. Cambridge University Press, 1996.
- [12] V. Jaunet and C. Braud. Experiments on lift dynamics and feedback control of a wind turbine blade section. *Renewable Energy*, 126:65–78, 2018.
- [13] J. Jeong and F. Hussain. On the identification of a vortex. *Journal of Fluid Mechanics*, 285:69–94, 1995.
- [14] R. T. Jones. The unsteady lift of a wing of finite aspect ratio. Technical Report NASA-R681, 1940.
- [15] M. Melius, R. B. Cal, and K. Mulleners. Dynamic stall of an experimental wind turbine blade. *Physics of Fluids*, 28(3):034103, 2016.
- [16] M. Michard, L. Graftieaux, L. Lollini, and N. Grosjean. Identification of vortical structures by a non local criterion- Application to PIV measurements and DNS-LES results of turbulent rotating flows. In *Symposium on Turbulent Shear Flows, 11 th*, Grenoble, France, 1997.
- [17] K. Mulleners and M. Raffel. The onset of dynamic stall revisited. *Experiments in Fluids*, 52(3):779–793, 2012.
- [18] K. Mulleners and M. Raffel. Dynamic stall development. *Experiments in Fluids*, 54(2), 2013.
- [19] G. Pechlivanoglou. *Passive and active flow control solutions for wind turbine blades*. PhD thesis, Technical University of Berlin, 2013.
- [20] M. M. Pedersen, T. J. Larsen, H. A. Madsen, and G. C. Larsen. Using wind speed from a blade-mounted flow sensor for power and load assessment on modern wind turbines. *Wind Energy Science*, 2(2):547–567, 2017.

- [21] T. F. Pedersen, N. N. Sørensen, and P. Enevoldsen. Aerodynamics and Characteristics of a Spinner Anemometer. *Journal of Physics: Conference Series*, 75:012018, 2007.
- [22] A. Rezaeiha, R. Pereira, and M. Kotsonis. Fluctuations of angle of attack and lift coefficient and the resultant fatigue loads for a large Horizontal Axis Wind turbine. *Renewable Energy*, 114:904–916, 2017.
- [23] L. Sirovich. *Turbulence and the dynamics of coherent structures. I - Coherent structures. II*, volume 45. 1987.
- [24] A. Soulier, D. Voisin, F. Danbon, and C. Braud. Electronic TellTale (E - penon) sensor to detect flow separation on wind-turbines blades. In *Wind Energy Science Conference*, DTU (Danemark), 2017. Wind Energy Science Conference.
- [25] N. Swytink-Binnema and D. A. Johnson. Digital tuft analysis of stall on operational wind turbines: Digital tuft analysis of stall on operational wind turbines. *Wind Energy*, 19(4):703–715, 2016.
- [26] N. Troldborg, C. Bak, H. A. Madsen, and W. R. Skrzypinski. DANAERO MW: Final Report. Technical report, DTU Wind Energy, 2013.
- [27] S. Yarusevych, P. E. Sullivan, and J. G. Kawall. On vortex shedding from an airfoil in low-Reynolds-number flows. *Journal of Fluid Mechanics*, 632:245, 2009.